




MXene-reduced graphene oxide sponge-based solar evaporators with integrated water-thermal management by anisotropic design

Zonglin Liu¹, Renjie Ding¹, Fuhua Xue¹, Xu Zhao¹, Zhong Chen¹ , Haowen Zheng¹, Pengyang Li¹, Qian Yan¹, Liangliang Xu¹, Jinhua Xiong¹, Qingyu Peng¹ [✉] & Xiaodong He¹ [✉]

The main issue limiting the performance of the solar evaporators is that water-thermal management is difficult to coordinate. Herein, we achieve integrated water-thermal management by designing hierarchical MXene-reduced graphene oxide sponges with anisotropic thermal conductivity and axial-directional water conveyance channels. The reduced graphene oxide acts as the sponge framework and carbon source for in situ synthesis of MXenes on the surface. The axial-oriented framework supports the structure and provides fast water transmission channels to the air-water interface. Meanwhile, the MXene nanosheets are vertically aligned on the framework surface, making the radial thermal conductivity of the sponges much greater than the axial one, which suppresses heat loss in the axial direction. The material exhibits an evaporation rate of $2.35 \text{ kg m}^{-2} \text{ h}^{-1}$ under one sunlight and maintains 85 % energy efficiency under weak sunlight (0.5-sun). Furthermore, the sponge shows a long working life with 96 % evaporation rate retention after a 30-day-sustained operation.

¹National Key Laboratory of Science and Technology on Advanced Composites in Special Environments, Center for Composite Materials and Structures, Harbin Institute of Technology, 150080 Harbin, P.R. China. ✉email: pengqingyu@hit.edu.cn; hexd@hit.edu.cn

Clean water is the cornerstone of human health and industry^{1–3}. However, water resources are not evenly distributed across the planet, and most exist as seawater that cannot be directly used^{1,4}. Therefore, it is vital to use green energy to supplement water resources through seawater desalination and sewage purification^{5–10}. As the representative of green energy, solar energy has been widely used in environmentally friendly and sustainable evaporation technology^{4,8–12}. Solar energy is converted into heat energy to accelerate water evaporation at the water–air interface by the solar steam generators floating on the water^{5,13}. The solar-thermal energy conversion mechanism mainly includes the local plasma effect of noble metal nanoparticles^{14,15}, non-radiative relaxation of semiconductors⁴, thermal vibration of molecules in carbon-based materials^{16,17}, etc. To enhance the solar-to-steam energy conversion efficiency, the solar evaporators are supposed to possess high photothermal conversion efficiency^{3,18–20}, water management supplying consecutive water for continuous evaporation, and thermal management suppressing heat loss^{21–24}. Compared with noble metal nanoparticles, carbon nanomaterials, such as reduced graphene oxide (rGO)^{18,21,25,26}, carbon nanotube (CNT)^{17,26–28}, MXene^{6,11,14,29,30}, etc., possess excellent solar-thermal energy conversion properties in the whole solar wavelength. Meanwhile, the structure and composition of the carbon-based composites can be adjusted for integrated water-thermal management^{31–33}. Therefore, carbon nanomaterials are widely used as precursors for efficient solar evaporators^{34–36}.

By selecting raw materials, good photothermal conversion efficiency can be achieved, but it is difficult to coordinate water and heat management. In fact, the water involved in the evaporation of the solar steam system is only a tiny part of the volume near the water–air interface^{4,5,37,38}. Thus, a consecutive flow of water is required to be transported to the air–water interface for continuous evaporation. However, thermal diffusion is inevitable during water transportation. There is always a part of solar-converted heat energy heating the water not directly involved in evaporation^{16,39,40}. Therefore, coordinating water transportation to the air–water interface while minimizing heat diffusion is challenging^{11,17,41}. Water management and thermal management conflict, and simple continuous micron vessels are challenging to meet both requirements. Therefore, to achieve integrated water-thermal management, it is necessary to design the evaporators' microstructure meticulously. In previous research, bionics (feathers¹¹, honeycomb¹⁹, mussel⁷, crumpled textures^{6,42}, continuous vertical vessels^{29,41}, etc.) is widely used to design the microstructure of the evaporators to realize the integrated management of water and heat. However, some issues still need to be addressed: 1. The solar steam generators cannot achieve passive integrated water-thermal management, which is not environmentally friendly^{13,39}. 2. The evaporation performance of the evaporators under weak light conditions still needs to be improved^{19,41}. 3. The structural design is not meticulous enough as part of the solar active nanomaterials (such as MXene, rGO, CNT, etc.) does not directly participate in solar energy absorption. Thus, the theoretical efficiency of the nanomaterials has been sacrificed^{25,29,31,42}. 4. The bottom-up assembly makes the MXene nanosheets unnecessarily exposed to the water–oxygen environment during the process, resulting in the oxidation of MXene and thus limiting the working life of MXene-based evaporators⁴³.

To tackle the above challenges, we fabricated the hierarchical MXene-rGO sponges (rGMX_n sponges). The axial thermal conductivity of the sponges is designed to be lower than the radial one. Therefore, the heat is more likely to spread in the radial plane rather than in the axial direction far away from the air–water interface. The in-plane temperature of the sponges is more likely to be homogenized, effectively preventing the local

steam pressure from reaching saturation⁶. Furthermore, the axial-oriented vessels in the sponges allow for continuous water transition. Thereby, the none-external-energy-input integrated water-thermal management is achieved.

In detail, the MXenes nanosheets are in situ synthesized perpendicularly on the surface of the sponges, which can maximize the exposure of MXene to the sunlight and acquire a high photothermal conversion efficiency. Besides, the rGMX_n-based evaporator is obtained by in situ etching of the MAX-based sponge. Therefore, the oxidation of MXene during the bottom-up assembly is avoided, greatly extending the working life of the rGMX_n-based evaporators. The low density, high hydrophilicity, and mechanical stability make the sponges float on the water as free-standing solar evaporators. Furthermore, the low density of sponges brings a very low thermal conductivity, effectively inhibiting the unnecessary diffusion of heat energy in water. The sponges obtained in this work have achieved water–thermal integrated management by anisotropic designing and possess good evaporation performance. The rGMX₅ sponge with MXene content of only ~4 mg ml^{−1} can achieve an evaporation rate of 2.35 kg m^{−2} h^{−1} and an efficiency of up to 127% under one sunlight illustration, and the rGMX₅ sponge maintains an evaporation rate of 1.6 kg m^{−2} h^{−1} with 85% energy efficiency even under weak sunlight (0.5-sun). Furthermore, the rGMX₅ sponge possesses an extraordinarily long working life with a 96% retention of evaporation rate after sustained operation for 30 days.

Results and discussion

Fabrication of the MXene-reduced graphene oxide sponges.

The MXene-sponge-based solar-driven evaporators are fabricated by in situ synthesis of MXene nanosheets on the surface of the rGO sponges (Fig. 1a, Supplementary Fig. 1)^{44,45}. At first, precursor sponges are obtained by directional freezing and freeze-drying. Subsequently, by sacrificing part of rGO as the carbon source, a uniform MAX phase layer is synthesized in situ on the surface of the rGO sponges. Finally, rGMX_n sponges are obtained with the MXene nanosheets vertically anchored on the rGO framework after in situ etching by acid. As there is no need for assembly after etching, the rGMX_n sponge can be immediately put into use, greatly shortening the exposure time of MXene in the water–oxygen environment during the fabrication process. Besides, without the need for solvent displacement³¹, the MXene nanosheets are barely self-restacked, guaranteeing the utilization of MXene in the photothermal conversion of solar energy.

In the rGMX_n sponges, the rGO framework supports the structure of the sponges. The axial-oriented vessels provide fast water transmission channels for continuous evaporation at the air–water interface (Fig. 1b). Unidirectional freezing causes the sponge's walls to have micro orientation and macro isotropy in the radial plane (Fig. 1c). Furthermore, the distribution of MXene nanosheets makes the radial thermal conductivity of the sponges much greater than that of the axial one. Therefore, the rGMX_n sponges have achieved efficient integrated water and thermal management, ensuring to be potential solar-driven evaporators.

Inspired by the coral, the MXene nanosheets are vertically synthesized in situ on the surface of the rGO framework (Fig. 1b). With the growth of MXene nanosheets, the (002) peak of the graphene phase in the rGMX_n sponges is gradually invisible in the X-ray diffraction (XRD) spectra, as the MXene nanosheets entirely covered the surface of the sponges (Fig. 1d). Besides, the disappearance of the 39° peak indicates that the aluminum in the MAX phase has been etched completely^{18,44,45}. With the increased content of MXene, the ratio of D peak (A_{1g} mode at ~1350 cm^{−1}) to G peak (E_{2g} mode at ~1590 cm^{−1}) in the Raman spectra decreases, indicating the symmetry break of the

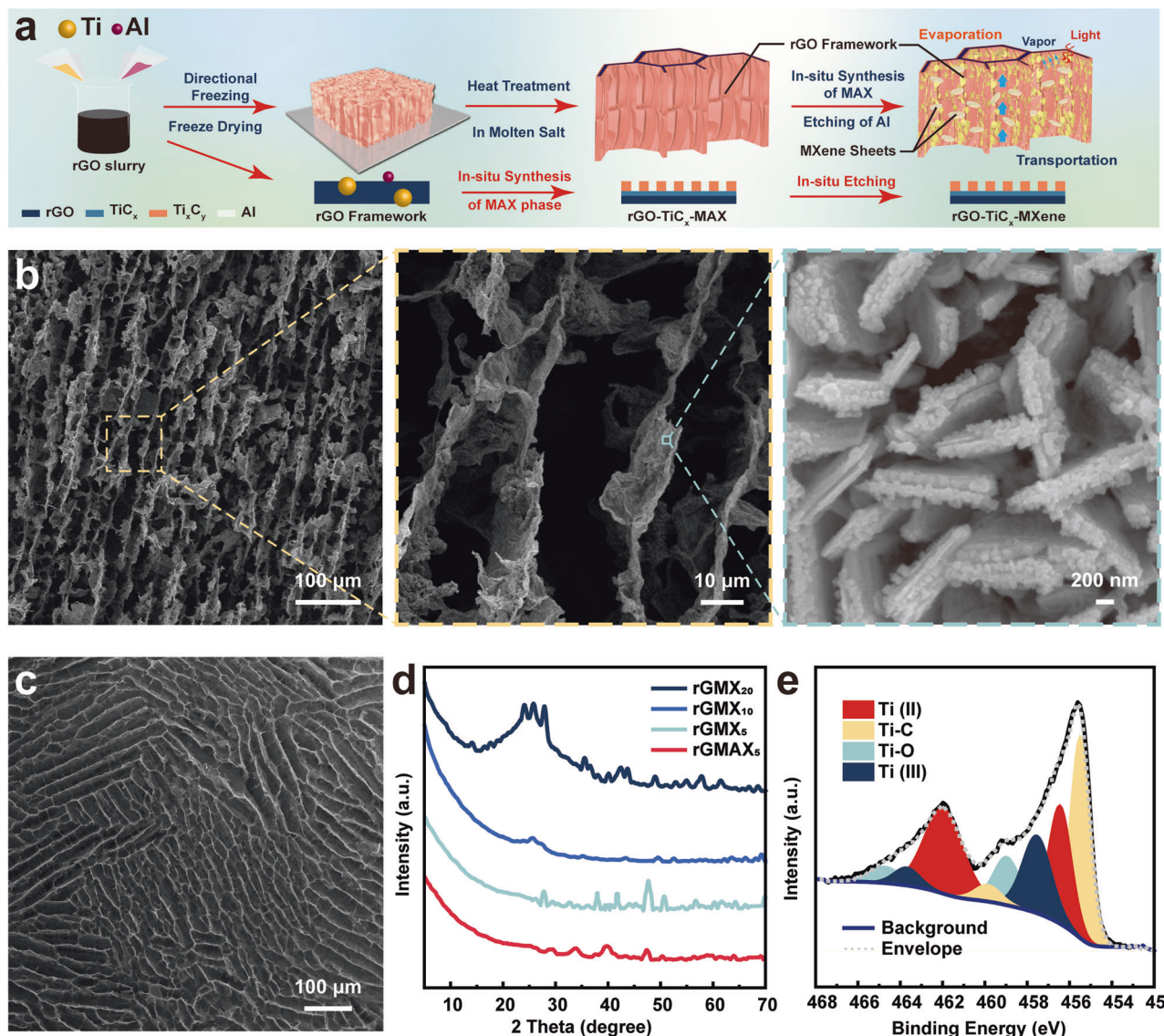


Fig. 1 Fabrication of rGMX_n sponges. **a** Schematic illustration of the synthesis of rGMX_n sponges. **b** Axial and **c** radial SEM images of rGMX_n sponges. **d** XRD patterns of rGMX_n and rGMX₅ sponges ($n = 5, 10$, and 20). **e** XPS Ti $2p$ spectra of rGMX₅ sponge.

microstructure of the sponges (Supplementary Fig. 2a)^{45,46}. Besides, the peaks at 610 , 410 , and 250 cm^{-1} represent the nonstoichiometric $\delta\text{-TiC}_x$ phases, indicating the MXenes in the rGMX_n sponges are a combination of Ti_2C and Ti_3C_2 ⁴⁷. The X-ray Photoelectron Spectroscopy (XPS) spectra have further proved this, as the Ti $2p$ XPS spectra (Fig. 1e, Supplementary Fig. 2) can be divided into four doublets located at 457.4 eV (reduced Ti ions), 454.5 eV (Ti–C bond), 455.9 eV (titanium oxy carbides and substoichiometric TiC_x , $x < 1$), and 458.8 eV (Ti^{4+} ions)^{26,48}.

Anisotropic mechanical performance of the sponges. The rGMX_n sponges obtained by directional freezing possess low density (Supplementary Table 1) but strong mechanical stability and anisotropic mechanical performance. The rGMX₅ sponge can support a thousandfold-dead-weight weight in the axial direction without macroscopic deformation (parallel to the freezing direction). At the same time, it is easy to be compressed in the radial direction, showing good elasticity (perpendicular to the freezing direction, Fig. 2a). The rGMX_n sponges' modulus along the axial direction is much greater than that in the radial direction due to the ice crystal's growth during oriented freezing (Fig. 2b,

Supplementary Fig. 3a, b). Furthermore, the rGMX_n sponge has a more extensive elastic deformation range in the radial direction with stable cyclic performance (Fig. 2c, Supplementary Fig. 3c–f).

The significant anisotropic mechanical performance and strong mechanical stability can be expressed as follows (Fig. 2e): The oriented rGO framework provides excellent compressive strength in the axial direction, while the axial-oriented vessels ensure the sponges with ample space for compression in the radial direction. Furthermore, the van der Waals force between the MXene sheets vertically anchored on the rGO framework offers the sponges good elasticity^{16,29,49}. It is worth pointing out that the modulus of the rGMX_n sponges drops with the increase of MXene content (Fig. 2b, Supplementary Fig. 3a, b), which is due to the synthesis mechanism: The in situ synthesis of the MAX phase has sacrificed part of the rGO as carbon source, which has introduced a lot of defects in the framework^{45,46,48}. The sponges can self-float on the water because of their excellent mechanical stability, low density, and good hydrophilicity. The stable mechanical properties of the rGMX_n sponges can ensure long-term operation and maintain their integrity after immersion in water. Due to the anisotropic modulus, the rGMX_n sponges can shrink in the radial direction

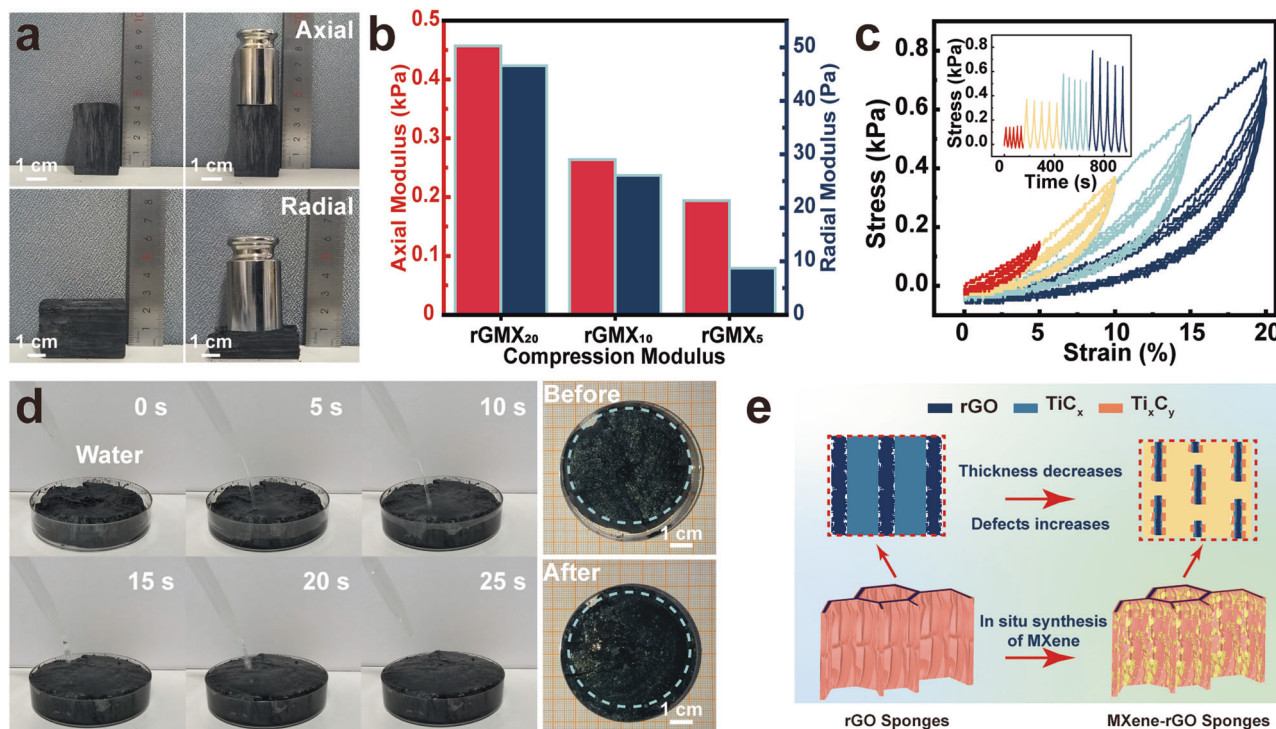


Fig. 2 Mechanical stability of rGMX_n sponges. **a** Digital image of anisotropic rGMX₅ sponge pressed by 200 g weight from different directions. **b** Anisotropic compressive modulus of rGMX_n sponges. **c** Mechanical stability performance of rGMX₁₀ sponges in the radial direction. **d** Digital images of rGMX₅ sponges during water immersion. **e** Schematic of the anisotropic mechanical mechanism of the sponges.

when losing water and expand back to their original volume, quickly responding to water absorption (Fig. 2d). The structure of the sponge is very stable, which can be well maintained after rapid water absorption cycles (Supplementary Video 1).

Anisotropic thermal performance of the sponges. The rGMX_n sponge has excellent thermal insulation performance due to its abundant porous structure^{18,50}. Separated by a one-cm-thick sponge over the baking of the alcohol lamp, the plantlets can remain upright within 60 s (Fig. 3a, Supplementary Fig. 6a, b). As the MXene content increases, the thermal conductivity of the sponge increases. The rGMX₅ sponge has an axial thermal conductivity of $0.025 \text{ W m}^{-1} \text{ K}^{-1}$ (Fig. 3b), while its radial thermal conductivity ($0.268 \text{ W m}^{-1} \text{ K}^{-1}$) is tenfold higher. The thermal conductivity demonstration experiment (Fig. 3c) intuitively reveals that the increase of MXene content has little effect on the axial thermal conductivity (Supplementary Fig. 4a) but dramatically improves the radial thermal conductivity (Supplementary Fig. 4b).

The smaller thermal conductivity of the rGMX_n sponges with anisotropy compared to rGO sponges can be explained as (Fig. 3d): 1. Due to directional freezing, the holes in the sponge are directionally arranged, resulting in anisotropic thermal conductivity of the sponge^{44,51}. 2. The heat transfer of sponges along the axial direction mainly comes from the heat conduction in the oriented rGO framework, as the continuous rGO framework possesses good theoretical thermal conductivity. However, the in-situ MAX phase growth has sacrificed a portion of rGO as the carbon source, disrupting the continuity of the framework. The heat conduction of the sponges along the framework is hindered. Therefore, the axial thermal conductivity of the rGMX_n sponge slumps and is lower than other aerogels (Supplementary Fig. 5a)^{11,16,51}. 3. The MXene sheets are perpendicular to the rGO framework, making it easy for heat to transfer from in-plane rGO to out of plane MXene with larger theoretical thermal conductivity, further decreasing the axial thermal conductivity of the

rGMX_n sponges. Meanwhile, the hierarchical structure has reduced the interfacial thermal resistance along the radial direction^{6,14}. Therefore, as the MXene content increases, the radial thermal conductivity of the sponge increases.

The impacts of structural design on sponge evaporation performance.

The outstanding absorption efficiency of sunlight is the prerequisite for achieving high solar-driven steam generation^{4–6}. After etching, the light absorption of rGMX_n sponges is greatly enhanced in the whole solar band, as the etching has increased the layer spacing of MXene sheets and the surface areas exposed to light (Supplementary Fig. 7a). Besides, the light absorption of sponges enhances with the increase of MXene content (Fig. 4a). When the light is incident from the axial direction, most of the light is absorbed and converted into heat energy by the MXene sheets, so the temperature of the top surface of the sponge rises rapidly (Fig. 4b)^{11,14,43}. Under one-sun illumination exposed to air, the central temperature of the upper surface of the rGMX₂₀ sponge increases rapidly from 22 to 55 °C within 10 s. The increase in MXene content improves the sponge's photothermal conversion efficiency, and the central temperature of the upper surface of the rGMX₅ sponge can reach 72 °C within 10 s ($\Delta T = 50$ °C, Fig. 4c). Moreover, a fast photothermal response rate is also of great importance for the evaporators^{12,21,27,28}. Therefore, the light (one-sun illumination) is turned off after 20 s of illumination (Supplementary Fig. 7b). After 10 s of illumination, the temperature distribution of the sponge tends to be stable and reaches a dynamic balance. The maximum temperature at the lateral surface of the sponges is lower than the temperature at the center of the top surface of the sponges. The temperature gradually decreases from top to bottom (Supplementary Fig. 7c). After the light is turned off, the sponge returns to its initial state after 20 s. In contrast, the temperature gradient from top to bottom is maintained in this process as the

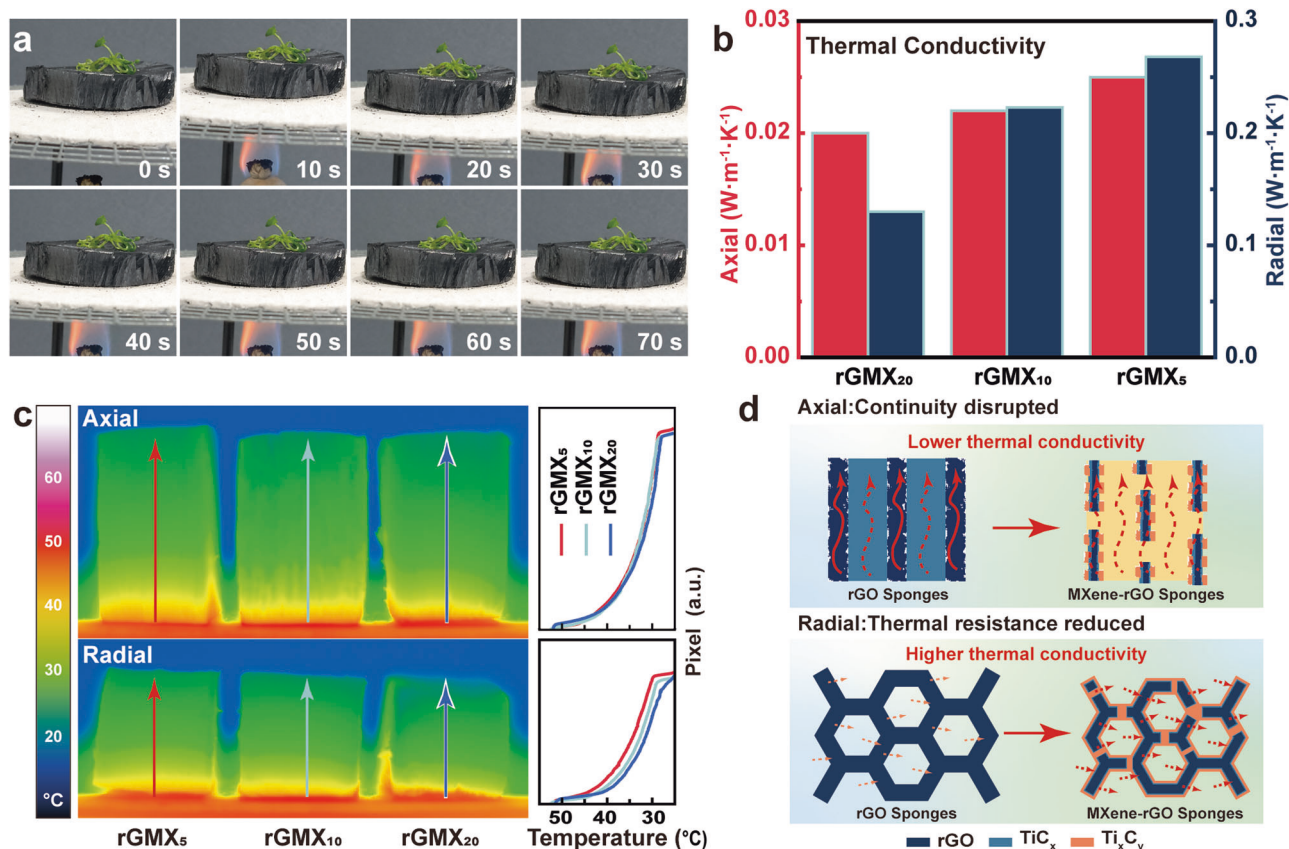


Fig. 3 Anisotropic thermal performance of rGMX_n sponges. **a** Digital image of a plantlet over an alcohol lamp flame separated by a thin rGMX₅ sponge. Anisotropic **b** thermal conductivity, **c** infrared thermal images, and **d** a schematic of the thermal mechanism of the sponges.

radial thermal conductivity of the sponge is far better than that of the axial direction.

The rGMX_n sponges can float on the water and be used as a free-standing photothermal water evaporation device due to their high hydrophilicity and low density, thus guaranteeing adequate water supply without excess supporting materials or external energy input (Fig. 4d, Supplementary Fig. 8a). The rGMX_n-sponge-based evaporators are tested under one-sun illumination (1.0 kW m⁻²) in the laboratory. The central temperature of the top surface of the rGMX₂₀ sponge immersed in water has increased by 10 °C when exposed to one-sun illumination for 5 min, while the rGMX₅ sponge with more MXene content has increased by 19 °C (Fig. 4e, f). Compared to exposure to the air (Fig. 4b), the relatively lower temperature is caused by the violent evaporation of water, carrying away most of the heat^{6,11,17,29}. The water evaporation rates of the rGMX_n sponges under one-sun illumination are 1.75 kg m⁻² h⁻¹ (rGMX₂₀), 1.95 kg m⁻² h⁻¹ (rGMX₁₀), and 2.35 kg m⁻² h⁻¹ (rGMX₅), respectively (Fig. 4g, Supplementary Fig. 8b). Due to etching, the MXene nanosheets form a large number of hydrogen bonds with water by the abundant hydrophilic functional groups (–OH, –F, etc.) on the surface, which significantly improve the hydrophilicity of the sponges and reduce the enthalpy of evaporation of water on the sponge surface (Supplementary Fig. 9a)^{18,25}. Raman spectra are used to investigate the hydratable interaction of the rGMX_n sponges (Supplementary Fig. 9b). The region of O–H stretching in the Raman spectra represents the form of hydrogen bonds: the peaks at 3514 and 3630 cm⁻¹ correspond to intermediate water (IW) with weak or non-hydrogen bonds, and the peaks at 3233 and 3401 cm⁻¹ could be associated with free water (FW) with four hydrogen bonds (two lone electron pairs and two

protons)^{17,52}. A lower proportion of FW predicates a lower energy demand for water vaporization. The IW/FW value of water in the rGMX₅ sponge reaches ca. 0.83, much larger than that of the rGMX₁₀ sponge (0.74), rGMX₂₀ sponge (0.69), and bulk water (0.29), indicating easier evaporation of water in the rGMX₅ sponge (Supplementary Fig. 9c)¹⁷. The hydration state is examined by the differential scanning calorimetry (DSC) method, and the theoretical enthalpy of water evaporation in the rGMX_n sponges is calculated through the DSC results (Supplementary Fig. 9d)^{7,18}. The photothermal evaporation efficiency of sponges is calculated according to the theoretical enthalpy (Fig. 4h). The rGMX₅ sponge with an evaporation rate of 2.35 kg m⁻² h⁻¹ under one-sun illumination possesses an evaporation efficiency of 127% with the MXene content of only ~4 mg ml⁻¹ (Supplementary Table 1), much superior to previously reported photothermal evaporators (Supplementary Fig. 5b)^{11,24,30,42}.

The continuous and effective evaporation efficiency of the rGMX_n sponges benefits from the excellent integrated water–thermal management and the mechanism can be explained as follows: 1. MXene and rGO nanosheets within the rGMX_n sponges possess high theoretical photothermal conversion efficiency in the whole frequency band of sunlight, ensuring sufficient heat energy for the evaporation of water in the sponges. Meanwhile, the MXene nanosheets vertically aligned on the rGO framework, dramatically enlarging the effective surface area of MXenes, further improving the photothermal conversion efficiency of sponges^{7,11,14}. Besides, the hierarchical microstructure makes the incident sunlight multi-reflect among the MXene nanosheets and the rGO framework, enhancing sunlight absorption^{31,50}. 2. The water management is accomplished by the sponges' axially oriented vessels, which offer fast channels for

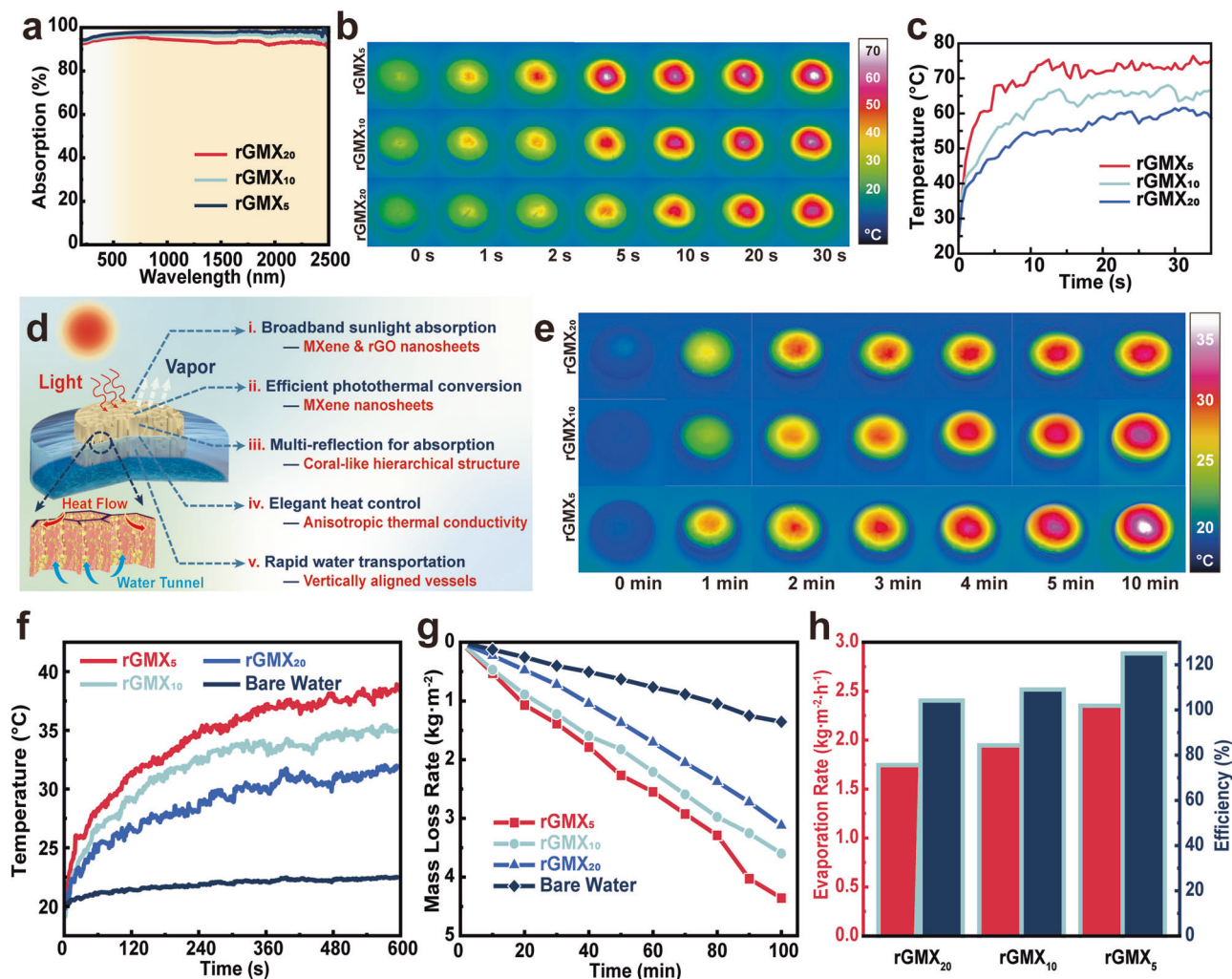


Fig. 4 Photothermal performance of rGMX_n sponges under one-sun illumination. **a** The light absorption spectra of rGMX_n sponges. **b** Infrared images and **c** temperature of the top surface of rGMX_n sponges under one-sun illumination exposed in the air for 30 s. **d** Schematic of the photothermal mechanism of rGMX_n sponges. **e** Infrared images and **f** temperature of the top surface of rGMX_n sponges under one-sun illumination floating on the water for 5 min. **g** Mass loss and **h** evaporation rate and efficiency of rGMX_n sponges under one-sun illumination.

water transfer from the bottom to the top (Supplementary Fig. 10)^{11,18,29}. 3. The heat regulation is achieved by the low anisotropic thermal conductivity of the sponges: the relatively better radial thermal conductivity makes the temperature of the top surface of the sponges tend to be homogenized, achieving a larger area to participate in effective evaporation; the relatively slower thermal diffusion along the axial direction reduces heat loss for heating unnecessary water not participating in evaporation (Supplementary Fig. 11)⁶. 4. The abundant hydrophilic functional groups (—F, —OH, etc.) on the sponge surface significantly reduce the surface tension of water, reducing the evaporation enthalpy of water in the sponges^{17,52,53}.

Evaporation performance of the sponges in actual environments.

As the natural sunlight usually is lower than 1-sun, evaporation performance under weak irradiance is also of practical importance. Therefore, the rGMX_n sponges are tested under weak sunlight of 0.3, 0.5, and 0.7-sun irradiance, respectively (Supplementary Fig. 12). The increase of MXene content dramatically improves the performance of the sponges under weak light. The rGMX₅ sponge possesses an evaporation rate of 2.1 kg m⁻² h⁻¹ (0.7-sun), 1.6 kg m⁻² h⁻¹ (0.5-sun), and 1.2 kg m⁻² h⁻¹ (0.3-sun), respectively, which are comparable to the previously reported state-

of-the-art evaporators^{4,11,43}. To further test the stability of the sponge under actual working conditions, especially under weak sunlight, the rGMX₅-sponge-based evaporator has been placed on a windowsill in the laboratory of Harbin Institute of Technology (HIT, Harbin, China). The system's mass change and solar intensity have been carefully recorded from 7:00 to 17:00 to evaluate the practical performance of the rGMX₅ sponges quantitatively (Fig. 5a). The system can yield 10.7 kg m⁻² purified water and possess an average evaporation rate of ~1 kg m⁻² h⁻¹ in a single day. Due to the in-situ synthesis and etching, the exposure of MXene in the water-oxygen environment is avoided during fabrication, thereby extending its working life. The rGMX₅ sponge exhibits a durable photothermal evaporation performance after sustained operation for ten days (Fig. 5b, Supplementary Fig. 13a). Furthermore, the rGMX_n sponge shows a long stable working life and has a photothermal evaporation efficiency (2.26 kg m⁻² h⁻¹) after being soaked in water for 30 days (Supplementary Figs. 13b and 14).

In actual scenarios, the working water environment of the evaporators is unpredictable. Therefore, the sponges need to be able to adapt to various extreme environments. The rGMX_n sponges possess strong mechanical stability and excellent hydrophily, ensuring they can be used as free-standing solar-driven evaporators floating on water. As expected, the rGMX₅ sponges

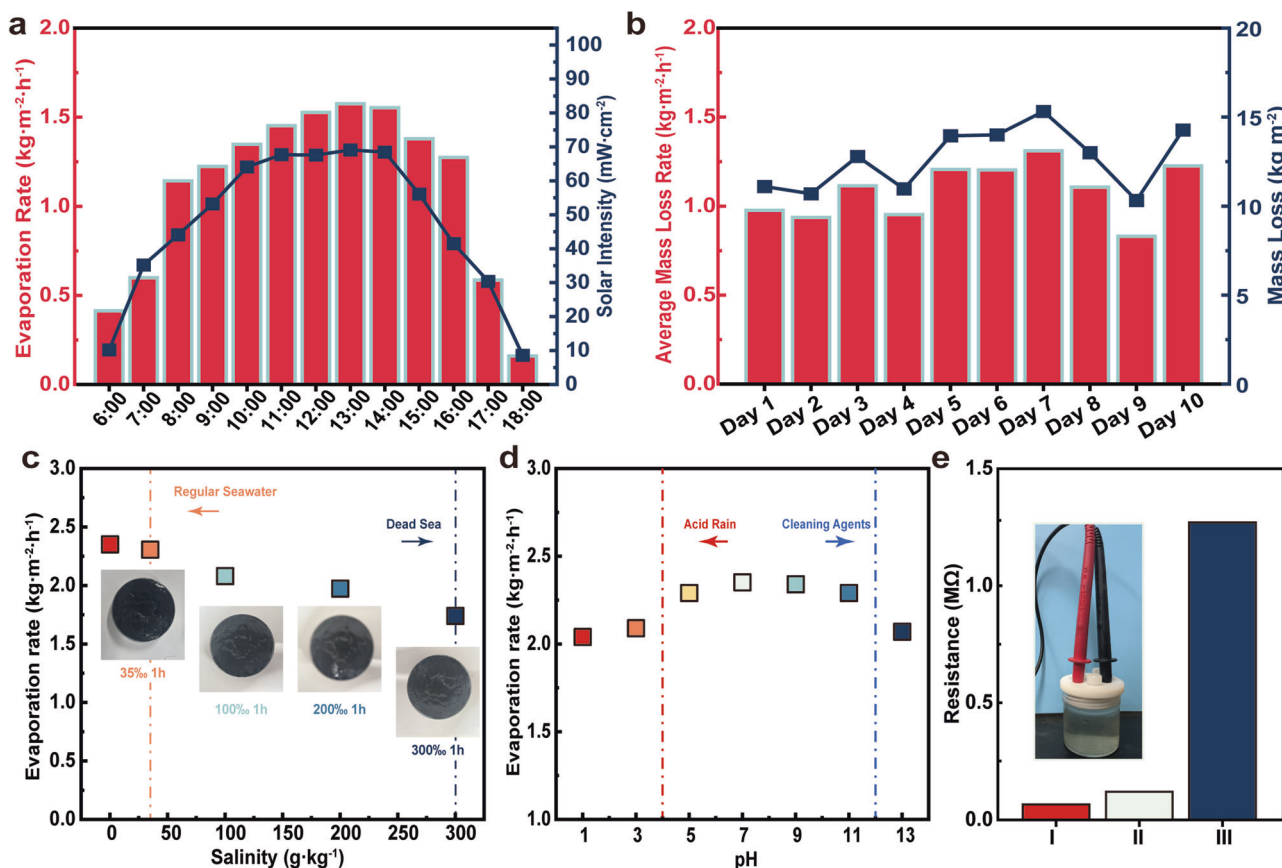


Fig. 5 Photothermal water evaporation performance of rGMX₅ sponges. **a** Synchronous solar intensity and water evaporation rates of rGMX₅ over time under a real sky. **b** Mass loss and average mass loss rate of rGMX₅ under a real sky for multi-days. Water evaporation rates of rGMX₅ sponge in **c** a wide range of salinity (inset images show no salt deposition on the surface of rGMX₅ sponge) and **d** a wide range of pH value. **e** Resistance of the water samples: I. Artificial seawater (salinity of 100‰); II. Water obtained from melting snow containing snow melting agent; III. Purified water of sample II (inset image shows the resistance test of water).

can maintain high evaporation efficiency under high salt conditions (Fig. 5c), with an evaporation rate of $1.75 \text{ kg m}^{-2} \text{ h}^{-1}$ in artificial seawater (300‰ salinity). Furthermore, the rGMX₅ sponges can bear acid rain (pH < 4) and cleaning agents (pH > 12) with an evaporation rate higher than $2 \text{ kg m}^{-2} \text{ h}^{-1}$ (Fig. 5d). Water obtained from melting snow containing snow-melting agents has been used to further prove the practicability of the rGMX_n sponges (Fig. 5e). After purification, the electrical resistance values obtained by a multimeter at a constant distance between electrodes increase from 120 kΩ to 1.27 MΩ, indicating improved water quality^{11,14,18,25}. The excellent salt crystallization resistance of rGMX_n sponges derives from two main factors. On the one hand, the MXene sheets are vertically aligned on the surface of the rGO framework, which greatly increases the MXene's interlayer spacing⁵⁴, accommodating more ions through intercalation^{55,56}. On the other hand, the abundant directional channels enable the sponges with good ion diffusion/transportation kinetics^{57,58} and diffuse concentrated salt down into the water¹⁴.

Conclusions

In summary, passive water-thermal integrated management is achieved by anisotropic designing of the microstructure of the MXene-rGO sponges. The MXene nanosheets in the rGMX_n sponges are in situ synthesized on the surface of the rGO framework, guaranteeing the sponges with high photothermal conversion efficiency in the whole solar wavelength. Furthermore, the sponges' axial-oriented vessels provide fast water transmission channels for continuous photothermal water evaporation at the

interface. The sponges' radial thermal conductivity ($0.268 \text{ W m}^{-1} \text{ K}^{-1}$) is much greater than that of the axial one ($0.025 \text{ W m}^{-1} \text{ K}^{-1}$), reducing the heat loss, thus achieving excellent water and thermal integrated management. The obtained rGMX_n sponges possess strong mechanical stability, low density, and excellent hydrophilicity and can be used as free-standing and durable steam generators floating on the water. Furthermore, the rGMX_n sponges have excellent solar energy utilization efficiency, especially in weak natural sunlight. At a weak solar irradiance of 0.5-sun, the rGMX₅ sponge has achieved an evaporation rate of $1.6 \text{ kg m}^{-2} \text{ h}^{-1}$ with an energy efficiency of 85%, illustrating potential applications for solar-driven water purification and desalination in the high-latitude water-deficient areas (under weak sunlight). The in-situ synthesis method proposed in this work paves an avenue for the low-cost realization of water and thermal integrated management of sponge-based solar-driven evaporators with easy deployment and long working life.

Methods

Materials. Titanium powders (Ti, 10 μm) were supplied by Beijing Xing Rong Yuan Technology Co., LTD, China. Aluminite powders (Al, purity of 99.9%, 300 mesh) were provided by Henan Yuanyang Powder Technology Co., Ltd., China. Sodium chloride (NaCl) and potassium chloride (KCl) were supplied by Tianli Chemical Reagent Co., Ltd., China. All the materials and chemicals were used without any treatment.

Synthesis of rGMX_n sponges. Take the rGMX₅ sponge as an example. 25 ml salt solution with 2.922 g NaCl and 3.95 g KCl was added dropwise to 100 ml concentrated GO slurry (6.25 mg ml⁻¹). Afterward, 0.09 g Al powders and 0.638 g Ti powders were added to the colloidal suspension, and the GO/Al/Ti slurry precursor of rGMX₅ was obtained. The precursor rGMX₅ slurry was then dropped into a Teflon mold for directional freezing with liquid nitrogen. After demolding, the frozen samples were kept in a freeze dryer for freeze-drying. Subsequently, the sponges were set in the tube furnace for heat treatment. With the protection of Ar gas, the tube furnace was heated to 500 °C at the rate of 3 °C min⁻¹ and kept for 1.5 h, then heated to 800 °C at the rate of 2 °C min⁻¹ and kept for 3 h, and then heated into 1100 °C with the rate of 3 °C min⁻¹ and kept for 1 h. After that, the tube furnace was cooled down to room temperature naturally. Thereby, the rGMX_n sponges with residual salts within were obtained. After that, the as-prepared rGMX_n sponges were etched with an acid solution (10 wt% HF and 10 wt% HCl) at 40 °C for 10 h. Thereby, the sponges were soaked in deionized water (DI) to remove acid, and then the rGMX_n sponges were obtained. The other rGMX_n sponges are prepared with the same method (Supplementary Table 2), except the amount of metal powder is different, which is determined by the molar ratio of Ti, Al, and C (4:1: n).

Characterization. Scanning electron microscope (FIB-SEM; TESCAN AMBER, Brno-Czech Republic) with an energy dispersive spectrometer (EDS) detector was employed to analyze the microstructure and elements distribution of obtained samples. X-ray diffraction (Bruker D2 Phaser, Germany) equipment with Cu K α radiation was used to measure the phase compositions of obtained samples ranging from 10° to 90° at a scan rate of 5° min⁻¹. XPS (ESCALAB 250, USA) and Raman (inVia-Reflex, UK) were carried out to record the spectra data. Mechanical tests were carried out by an instrument (Instron 5944) equipped with two flat-surface compression stages and a 2000 N load cell. The anisotropic thermal conductivities of the sponges were measured using an LFA467 (NETZSCH, Germany). The sunlight absorption spectra of the sponges were measured using a UV-vis-NIR spectrophotometer (UV3600i Plus, Shimadzu, Japan). The enthalpy of evaporation of water in the sponges was calculated based on differential scanning calorimeter (DSC) data collected by a thermogravimetry-differential scanning calorimetry system (NETZSCH STA 449F3, Germany) in a nitrogen environment.

Solar-driven vapor generation experiments. The water to be purified was held in an acrylic petri dish, and the rGMX_n sponges were self-floated on the water surface. The illumination was applied using a light source (CEL-HXUV300), and the solar intensity was measured by a solar power meter (CEL-NP2000-2(10)A, Beijing Zhongjiao Jinyuan Technology Co., Ltd). The mass change of water was recorded every hour by an electronic mass balance (at an accuracy of 0.1 mg), while the temperature change was monitored by a Thermal Imager (VarioCAM HD head, Germany). The room temperature is 20 °C with humidity at 40% in the laboratory. The actual solar-driven evaporation of sponges was carried out indoors under natural sunlight for ten consecutive days from 7 to 16 March 2023 in Harbin.

Data availability

The authors declare that all the relevant data are available within the paper and its Supplementary Information file or from the corresponding author upon reasonable request.

Received: 18 April 2023; Accepted: 23 August 2023;

Published online: 05 September 2023

References

- Lotfy, H. R., Staš, J. & Roubík, H. Renewable energy powered membrane desalination—review of recent development. *Environ. Sci. Pollut. Res. Int.* **29**, 46552–46568 (2022).
- Lin, S. et al. Seawater desalination technology and engineering in China: a review. *Desalination* **498**, 114728 (2021).
- Yang, L. et al. Marine biomass-derived composite aerogels for efficient and durable solar-driven interfacial evaporation and desalination. *Chem. Eng. J.* **417**, 128051 (2021).
- Zhao, F., Guo, Y., Zhou, X., Shi, W. & Yu, G. Materials for solar-powered water evaporation. *Nat. Rev. Mater.* **5**, 388–401 (2020).
- Tao, P. et al. Solar-driven interfacial evaporation. *Nat. Energy* **3**, 1031–1041 (2018).
- Ding, R. et al. Skin inspired multifunctional crumpled Ti₃T₂T_x MXene/tissue composite film. *Composites Part A-Appl. Sci. Manuf.* **158**, 106967 (2022).
- Zou, Y. et al. A mussel-inspired polydopamine-filled cellulose aerogel for solar-enabled water remediation. *ACS Appl. Mater. Interfaces* **13**, 7617–7624 (2021).
- Meng, S. et al. A customized kinetic energy harvesting system with multilayer piezoelectric membrane for solar interfacial vapor generation. *Nano Energy* **104**, 107996 (2022).
- Meng, S., Tang, C. Y., Yang, J., Yang, M. B. & Yang, W. A wave-driven piezoelectrical film for interfacial steam generation: beyond the limitation of hydrogel. *Adv. Sci. Weinh.* **9**, e2204187 (2022).
- Meng, S. et al. A wave-driven piezoelectric solar evaporator for water purification. *Adv. Energy Mater.* **12**, 2200087 (2022).
- Zhang, H. et al. Integrated water and thermal managements in bioinspired hierarchical MXene aerogels for highly efficient solar-powered water evaporation. *Adv. Funct. Mater.* **32**, 2111794 (2022).
- Zhang, Y. et al. Robust, scalable, and cost-effective surface carbonized pulp foam for highly efficient solar steam generation. *ACS Appl. Mater. Interfaces* **15**, 7414–7426 (2023).
- Zhao, F. et al. Highly efficient solar vapour generation via hierarchically nanostructured gels. *Nat. Nanotechnol.* **13**, 489–495 (2018).
- Fan, X. et al. A MXene-based hierarchical design enabling highly efficient and stable solar-water desalination with good salt resistance. *Adv. Funct. Mater.* **30**, 2007110 (2020).
- Chen, J. et al. Integrated evaporator for efficient solar-driven interfacial steam generation. *Nano Lett.* **20**, 6051–6058 (2020).
- Chen, Y. et al. Wood-inspired anisotropic cellulose nanofibril composite sponges for multifunctional applications. *ACS Appl. Mater. Interfaces* **12**, 35513–35522 (2020).
- Zhao, L. et al. Boosting solar-powered interfacial water evaporation by architecting 3D interconnected polymeric network in CNT cellular structure. *Chem. Eng. J.* **451**, 138676 (2023).
- Li, W. et al. Ultrahigh solar steam generation rate of a vertically aligned reduced graphene oxide foam realized by dynamic compression. *J. Mater. Chem. A* **9**, 14859–14867 (2021).
- Lei, Z. et al. Nature inspired MXene-decorated 3D honeycomb-fabric architectures toward efficient water desalination and salt harvesting. *Nanomicro Lett.* **14**, 10 (2021).
- Menon, A. K., Haechler, I., Kaur, S., Lubner, S. & Prasher, R. S. Enhanced solar evaporation using a photo-thermal umbrella for wastewater management. *Nat. Sustain.* **3**, 144–151 (2020).
- Ito, Y. et al. Multifunctional porous graphene for high-efficiency steam generation by heat localization. *Adv. Mater. Weinh.* **27**, 4302–4307 (2015).
- Xu, N. et al. Mushrooms as efficient solar steam-generation devices. *Adv. Mater. Weinh.* **29**, 1606762 (2017).
- Xu, Y. et al. Harvesting solar energy by flowerlike carbon cloth nanocomposites for simultaneous generation of clean water and electricity. *ACS Appl. Mater. Interfaces* **13**, 27129–27139 (2021).
- Liu, X. et al. Bifunctional, moth-eye-like nanostructured black titania nanocomposites for solar-driven clean water generation. *ACS Appl. Mater. Interfaces* **10**, 39661–39669 (2018).
- Li, X. et al. Reshapeable MXene/graphene oxide/polyaniline plastic hybrids with patternable surfaces for highly efficient solar-driven water purification. *Adv. Funct. Mater.* **32**, 2110636 (2022).
- Zhang, S. et al. Multiscale preparation of graphene oxide/carbon nanotube-based membrane evaporators by a spray method for efficient solar steam generation. *ACS Appl. Nano Mater.* **5**, 7198–7207 (2022).
- Han, S. et al. Flame synthesis of superhydrophilic carbon nanotubes/Ni foam decorated with Fe(2)O(3) nanoparticles for water purification via solar steam generation. *ACS Appl. Mater. Interfaces* **12**, 13229–13238 (2020).

28. Zhu, L., Ding, T., Gao, M., Peh, C. K. N. & Ho, G. W. Shape conformal and thermal insulative organic solar absorber sponge for photothermal water evaporation and thermoelectric power generation. *Adv. Energy Mater.* **9**, 1900250 (2019).
29. Pu, L. et al. Xylem-inspired polyimide/MXene aerogels with radial lamellar architectures for highly sensitive strain detection and efficient solar steam generation. *Nano Lett.* **22**, 4560–4568 (2022).
30. Zha, X. J. et al. Flexible anti-biofouling MXene/cellulose fibrous membrane for sustainable solar-driven water purification. *ACS Appl. Mater. Interfaces* **11**, 36589–36597 (2019).
31. Li, W. et al. Vertically aligned reduced graphene oxide/Ti₃C₂T_x MXene hybrid hydrogel for highly efficient solar steam generation. *Nano Res.* **13**, 3048–3056 (2020).
32. Mu, P. et al. Superwetting monolithic hollow-carbon-nanotubes aerogels with hierarchically nanoporous structure for efficient solar steam generation. *Adv. Energy Mater.* **9**, 1802158 (2019).
33. Ren, H. et al. Hierarchical graphene foam for efficient omnidirectional solar-thermal energy conversion. *Adv. Mater. Wein.* **29**, 1702590 (2017).
34. Ghasemi, H. et al. Solar steam generation by heat localization. *Nat. Commun.* **5**, 4449 (2014).
35. Li, Y. et al. 3d-printed, all-in-one evaporator for high-efficiency solar steam generation under 1 sun illumination. *Adv. Mater. Wein.* **29**, 1700981 (2017).
36. Xu, W. et al. Flexible and salt resistant Janus absorbers by electrospinning for stable and efficient solar desalination. *Adv. Energy Mater.* **8**, 1702884 (2018).
37. Zhu, M. et al. Dome-arrayed chitosan/PVA hydrogel-based solar evaporator for steam generation. *Sci. Rep.* **12**, 4403 (2022).
38. Shi, Y., Ilic, O., Atwater, H. A. & Greer, J. R. All-day fresh water harvesting by microstructured hydrogel membranes. *Nat. Commun.* **12**, 2797 (2021).
39. Zhang, Q. et al. Vertically aligned Janus MXene-based aerogels for solar desalination with high efficiency and salt resistance. *ACS Nano* **13**, 13196–13207 (2019).
40. Zhang, L. et al. Highly efficient and salt rejecting solar evaporation via a wick-free confined water layer. *Nat. Commun.* **13**, 849 (2022).
41. Wang, Z., Zhu, Y., Chen, Y., Yu, H. & Xiong, Z. Bioinspired aerogel with vertically ordered channels and low water evaporation enthalpy for high-efficiency salt-rejecting solar seawater desalination and wastewater purification. *Small* **19**, 2206917 (2023).
42. Li, K. et al. Biomimetic MXene textures with enhanced light-to-heat conversion for solar steam generation and wearable thermal management. *Adv. Energy Mater.* **9**, 1901687 (2019).
43. Xu, D., Li, Z., Li, L. & Wang, J. Insights into the photothermal conversion of 2D MXene nanomaterials: synthesis, mechanism, and applications. *Adv. Funct. Mater.* **30**, 2000712 (2020).
44. Liu, Z. et al. Anti-stacking synthesis of MXene-reduced graphene oxide sponges for aqueous zinc-ion hybrid supercapacitor with improved performance. *J. Mater. Sci. Technol.* **154**, 22–29 (2023).
45. Li, M., Han, M., Jie, Z., Deng, Q. & Huang, Q. Novel scale-like structures of graphite/ti₃c₂ hybrids for electromagnetic absorption. *Cancer* **4**, 800 (2018).
46. Li, X. et al. 2D carbide MXene t₂CT_x as a novel high-performance electromagnetic interference shielding material. *Carbon* **146**, 210 (2019).
47. Rakhi, R. B., Ahmed, B., Hedhili, M. N., Anjum, D. H. & Alshareef, H. N. Effect of Postetch annealing gas composition on the structural and electrochemical properties of ti₂ct_x MXene electrodes for supercapacitor applications. *Chem. Mater.* **27**, 5314–5323 (2015).
48. Li, X. et al. Vertically aligned sn⁴⁺ preintercalated Ti₂CT_x MXene sphere with enhanced Zn ion transportation and superior cycle lifespan. *Adv. Energy Mater.* **10**, 2001394 (2020).
49. Jia, C. et al. Highly compressible and anisotropic lamellar ceramic sponges with superior thermal insulation and acoustic absorption performances. *Nat. Commun.* **11**, 3732 (2020).
50. Lu, Y. et al. Surface patterning of two-dimensional nanostructure-embedded photothermal hydrogels for high-yield solar steam generation. *ACS Nano* **15**, 10366–10376 (2021).
51. Peng, Q. et al. Superlight, mechanically flexible, thermally superinsulating, and antifrosting anisotropic nanocomposite foam based on hierarchical graphene oxide assembly. *ACS Appl. Mater. Interfaces* **9**, 44010–44017 (2017).
52. Sekine, Y. & Ikeda-Fukazawa, T. Structural changes of water in a hydrogel during dehydration. *J. Chem. Phys.* **130**, 034501 (2009).
53. Monosmith, W. B. & Walrafen, G. E. Temperature dependence of the Raman OH-stretching overtone from liquid water. *J. Chem. Phys.* **81**, 669–674 (1984).
54. Yan, J. et al. Flexible MXene/graphene films for ultrafast supercapacitors with outstanding volumetric capacitance. *Adv. Funct. Mater.* **27**, 1701264–1701264 (2017).
55. Wang, X., Wan, K., Xie, P., Miao, Y. & Liu, Z. Ultralight, high capacitance, mechanically strong graphene-cellulose aerogels. *Molecules* **26**, 4891 (2021).
56. Naguib, M., Mochalin, V. N., Barsoum, M. W. & Gogotsi, Y. 25th anniversary article: MXenes: a new family of two-dimensional materials. *Adv. Mater. Wein.* **26**, 992–1005 (2014).
57. Huang, X., Huang, J., Yang, D. & Wu, P. A multi-scale structural engineering strategy for high-performance MXene hydrogel supercapacitor electrode. *Adv. Sci. (Weinh.)* **8**, 2101664 (2021).
58. Pan, Q. et al. Hierarchical vertically aligned titanium carbide (MXene) array for flexible all-solid-state supercapacitor with high volumetric capacitance. *ACS Appl. Energy Mater.* **2**, 6834–6840 (2019).

Acknowledgements

Supported by the Fundamental Research Funds for the Central Universities and Heilongjiang Provincial Natural Science Foundation of China (Grant No. YQ2020E009).

Author contributions

Z.L. and X.Z. conceived the idea of this work. Z.L., J.X., Z.C. and P.L. performed the experiments. Z.L., F.X. and H.Z. performed the measurement. Z.L. and R.D. performed the data analysis. X.H. and Q.P. supervised the whole work. Z.L. and X.W. analyzed the results. Z.L. and Q.P. wrote the manuscript. Q.Y. and L.X. helped improve the manuscript.

Competing interests

The authors declare no competing interests.

Additional information

Supplementary information The online version contains supplementary material available at <https://doi.org/10.1038/s43246-023-00398-9>.

Correspondence and requests for materials should be addressed to Qingyu Peng or Xiaodong He.

Peer review information *Communications Materials* thanks the anonymous reviewers for their contribution to the peer review of this work. Primary Handling Editors: Jet-Sing Lee.

Reprints and permission information is available at <http://www.nature.com/reprints>

Publisher's note Springer Nature remains neutral with regard to jurisdictional claims in published maps and institutional affiliations.



Open Access This article is licensed under a Creative Commons Attribution 4.0 International License, which permits use, sharing, adaptation, distribution and reproduction in any medium or format, as long as you give appropriate credit to the original author(s) and the source, provide a link to the Creative Commons license, and indicate if changes were made. The images or other third party material in this article are included in the article's Creative Commons license, unless indicated otherwise in a credit line to the material. If material is not included in the article's Creative Commons license and your intended use is not permitted by statutory regulation or exceeds the permitted use, you will need to obtain permission directly from the copyright holder. To view a copy of this license, visit <http://creativecommons.org/licenses/by/4.0/>.

© The Author(s) 2023